

# Riemann-Hilbert problems for the shapes formed by bodies dissolving, melting, and eroding in fluid flows

M. Nicholas J. Moore\*

Florida State University

## Abstract

The classical Stefan problem involves the motion of boundaries during phase transition, but this process can be greatly complicated by the presence of a fluid flow. Here, we consider a body undergoing material loss due to either dissolution (from molecular diffusion), melting (from thermodynamic phase change), or erosion (from fluid-mechanical stresses) in a fast-flowing fluid. In each case, the task of finding the shape formed by the shrinking body can be posed as a singular Riemann-Hilbert problem. A class of exact solutions captures the rounded surfaces formed during dissolution/melting, as well as the angular features formed during erosion, thus unifying these different physical processes under a common framework. This study, which merges boundary-layer theory, separated-flow theory, and Riemann-Hilbert analysis, represents a rare instance of an exactly solvable model for high-speed fluid flows with free boundaries.

## 1 Introduction

The classical Stefan problem of tracking a phase-change interface is one of great historical [57, 51, 11] and modern [20, 35, 24] significance in the mathematical and physical sciences. These moving-boundary problems not only apply to the melting/freezing of ice as originally introduced [57, 15, 55, 35], but also to the solidification of metal alloys [28, 5], the dissolution of chemical and pharmaceutical products [40, 19], and the creation of geological landscapes and patterns by erosion, dissolution, and aggregation [54, 38, 10, 36, 48].

These processes, however, often occur in conjunction with a fluid flow, driven either externally [40, 36, 48] or by density variations resulting from the phase change itself [59, 28, 55, 29]. Such flows can profoundly influence morphology by altering the nature of thermal or material transport from a simple diffusion process to advection-diffusion. Accordingly, the linear partial differential equations (PDEs) governing diffusion must be coupled to the typically nonlinear and nonlocal PDEs governing the fluid flow. In face of this complexity, many researchers have recognized the value in studying such processes from certain canonical settings [25, 50, 42, 27, 36, 52, 41], much like the classical Stefan problems of planar, cylindrical, or spherical bodies melting in a stagnant liquid [51, 11].

Recent laboratory experiments have examined how dissolvable and erodible bodies can be sculpted by fast flowing water [27, 50, 42]. Both cases show the emergence of self-similar dynamics:

---

\*Email addresses for correspondence: moore@math.fsu.edu, nickmoore83@gmail.com

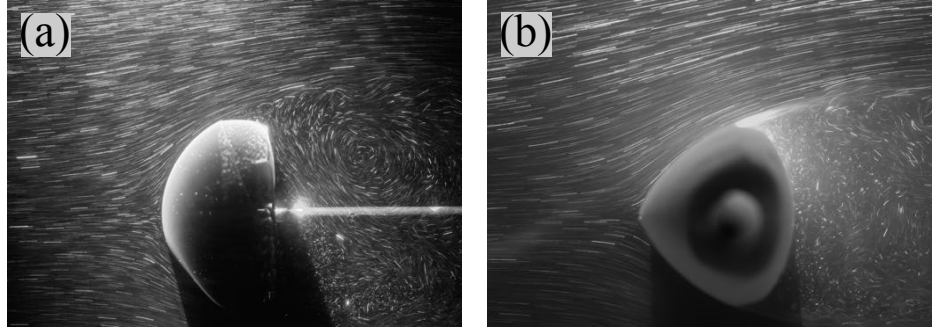


Figure 1: Experimental images of the morphologies formed by (a) dissolution and (b) erosion in fast flowing water. The dissolving body maintains a rounded front surface while the eroding body forms an angle at the nose. In each case, the flow (left to right) is on the order of 50 cm/s and the body scale is a few centimeters, yielding Reynolds numbers on the order of 10,000. Streakline photography is used to visualize this surrounding fluid flow. Figure adapted from (a) Huang et al. 2015 [27] and (b) Moore et al. 2013 [42] with permission.

regardless of initial conditions, the body converges to an equilibrium shape that is maintained by the fluid-structure coupling even as the body continues to shrink and ultimately vanishes. However, the equilibrium shapes resulting from dissolution and erosion show distinct differences. Dissolvable bodies (e.g. composed of sugar) form smooth, rounded front surfaces [27], while erodible ones (e.g. soft clay) develop sharp, angular features [50, 42], as shown in Figs. 1(a) and (b) respectively. The underlying reason for these different morphologies is the mechanism of material transport. Dissolution is caused by (flow-enhanced) molecular diffusion of solid material into the solvent, while erosion results from fluid shear stresses mechanically removing surface particles. In both cases, though, the emergent morphology is the one for which material removal is *uniform* along the surface, thereby offering a principle to unify such processes [27, 50, 42].

In the case of erosion, specifically, an initially cylindrical body was observed to develop a right angle at its front while vanishing. The terminal body thus resembled a wedge pointing upstream, with an attached boundary layer along its front portion and a complex flow structure in the wake (see Fig. 1(b)). The 90° opening angle was accurately predicted using Prandtl boundary-layer theory [50], though the portion further from the nose had to be simulated numerically using a separated-flow model called free-streamline theory [42].

These same ideas were applied to the case of a dissolving body [27] and, in that context, gave rise to a so-called Riemann-Hilbert (RH) problem<sup>1</sup> [1, 43]. An exact solution described the *entire* front surface of the terminal body, from the front stagnation point to the point of flow separation. This prediction agreed closely with experimental measurements and, incidentally, also resembled shapes observed in melting experiments [25], thus raising the question of whether similar techniques could be applied to other processes of flow-induced material removal.

In this paper we show that dissolution, melting, and erosion can all be linked under the RH framework through a one-parameter family of exact solutions. We provide a complete treatment

<sup>1</sup>RH problems, most commonly associated with integrable systems, are an active area of study due to their rich mathematical structure and the range of applications in which they appear [17, 18, 16, 31, 34, 37, 12, 44, 45], including applications in fluid mechanics [56, 6, 7, 8, 60, 62, 13].

of the underlying RH analysis, which covers as a special case the solution from Huang et al. 2015 (where the derivation was not given) [27]. Compared to dissolution, melting yields an identical RH problem, but erosion gives a problem that differs in the strength of a logarithmic singularity present in the boundary conditions. This singularity controls the opening angle of the equilibrium geometry. As such, a class of exact solutions can capture both the rounded surfaces formed by dissolution/melting and the angular features shaped by erosion, thus linking these very different morphologies through a common theory. The analysis relies on a novel combination of boundary-layer, separated-flow, and Riemann-Hilbert techniques.

The paper is organized as follows. In section 2 we introduce the physical models for dissolution, melting, and erosion, and in section 3 we discuss the Prandtl model used to describe the surrounding fluid flow. This model decomposes the velocity field into an inviscid outer component and a viscous boundary-layer component. Importantly, we use a model that accounts for flow separation. In section 4, we use boundary-layer analysis to derive conditions for self-similar shrinking during dissolution, melting, and erosion. In section 5, we introduce free-streamline theory to describe the outer, separated flow. We then use the self-similar conditions from section 4 to obtain a class of singular RH problems for the equilibrium shapes. In section 6 we derive exact solutions to the RH problems, and in section 7 we discuss the resulting morphologies as they compare to laboratory experiments.

## 2 Modeling dissolution, melting, and erosion in flow

In this section, we discuss the physical models for flow-driven dissolution, melting, and erosion. As in the experiments of [50, 42, 27], we consider a solid body (of length scale  $a$ ) held fixed against a fast-flowing fluid. The surrounding flow is governed by the incompressible Navier-Stokes equations,

$$\frac{\partial \mathbf{u}}{\partial t} + (\mathbf{u} \cdot \nabla) \mathbf{u} = -\frac{1}{\rho} \nabla p + \nu \nabla^2 \mathbf{u}, \quad (1)$$

$$\nabla \cdot \mathbf{u} = 0, \quad (2)$$

which we consider in two spatial dimensions  $\mathbf{x} = (x, y)$ . Here,  $\mathbf{u}$  is the velocity field,  $p$  is the pressure,  $\rho$  is the fluid density, and  $\nu$  is the kinematic viscosity. We assume the free-stream velocity  $U_0$  is sufficiently fast so that the Reynolds number is large,  $\text{Re} = aU_0/\nu \gg 1$ . On the surface of the body  $\partial B$ , we use  $(s, n)$  to denote the tangential and normal coordinates (see Fig. 2). Exploiting the fact that dissolution, melting, and erosion occur slowly compared to the flow timescale, we set  $\partial_t \mathbf{u} = 0$  above. This assumption implies that the velocity vanishes on the body surface. In addition, the flow must match  $U_0$  in the far field, giving the conditions

$$\mathbf{u} = 0 \quad \text{on } \partial B, \quad (3)$$

$$\mathbf{u} \rightarrow (U_0, 0) \quad \text{as } |\mathbf{x}| \rightarrow \infty. \quad (4)$$

The material comprising the body (e.g. sugar, ice, clay) determines whether dissolution, melting, or erosion occurs. In each case, the fluid flow determined by Eqs. (1)–(4) dictates the local rate of mass loss through either direct material transport (dissolution), thermal transport (melting), or mechanical shear stress (erosion). This loss rate can be quantified by the normal velocity  $V_n$  of the solid-fluid interface.

For dissolution, the interface velocity  $V_n^{(D)}$  is given by Fick's law for the solute concentration field  $C$ ,

$$V_n^{(D)} = D \frac{\partial C}{\partial n} \Big|_{\partial B}, \quad (5)$$

where  $D$  is the molecular diffusivity. The solute is transported by advection and diffusion, and subject to boundary conditions on the body and in the far field,

$$\frac{\partial C}{\partial t} + \mathbf{u} \cdot \nabla C = D \nabla^2 C, \quad (6)$$

$$C = 1 \quad \text{on } \partial B, \quad (7)$$

$$C \rightarrow 0 \quad \text{as } |\mathbf{x}| \rightarrow \infty. \quad (8)$$

Melting, on the other hand, is a phase transition associated with *thermal* transport. This process can be described in an analogous way, with the interface velocity  $V_n^{(M)}$  given by Fick's law for  $T$  the temperature field in the fluid [11],

$$V_n^{(M)} = -\frac{\alpha c_p}{L} \frac{\partial T}{\partial n} \Big|_{\partial B}. \quad (9)$$

Here,  $\alpha$  is the thermal diffusivity,  $L$  is the latent heat required for phase change, and  $c_p$  is the specific heat capacity of the fluid. The temperature field, much like solute concentration, is transported by advection and diffusion, but heat may also be created by viscous dissipation [11], giving

$$\frac{\partial T}{\partial t} + \mathbf{u} \cdot \nabla T = \alpha \nabla^2 T + \frac{\Phi_\mu}{\rho c_p}, \quad (10)$$

$$T = T_0 \quad \text{on } \partial B, \quad (11)$$

$$T \rightarrow T_0 + \Delta T \quad \text{as } |\mathbf{x}| \rightarrow \infty. \quad (12)$$

Here,  $T_0$  is the melting temperature of the solid body and  $T_0 + \Delta T$  is the far-field temperature. The amount of viscous dissipation is  $\Phi_\mu = \nabla \cdot (\boldsymbol{\tau} \mathbf{u}) - \mathbf{u} \nabla \cdot \boldsymbol{\tau}$ , where  $\boldsymbol{\tau} = \mu (\nabla \mathbf{u} + \nabla \mathbf{u}^T)$  is the viscous stress tensor and  $\mu = \nu \rho$  is the fluid's *dynamic* viscosity. We have neglected thermal-expansion and surface-tension effects, both of which are small in the laboratory experiments that motivate the current work [25, 50, 42, 27].

Erosion, in contrast, results from the removal of solid particles by fluid-mechanical shear stress [50, 23, 46]. The shear stress on the body surface is given by [49, 53]

$$\tau_s = \mu \frac{\partial u}{\partial n} \Big|_{\partial B}, \quad (13)$$

where  $u$  is the velocity component tangential to the surface. The interface velocity for erosion is then given by [50]

$$V_n^{(E)} = -C_E |\tau_s|, \quad (14)$$

where  $C_E$  is a (material-dependent) proportionality constant. Depending on the application, this law is sometimes modified to include a threshold stress value and, occasionally, a power on the shear stress [23, 46]. However, for the case of soft clay eroding in a high-Reynolds-number flow (order  $\text{Re} = 10,000$ ), Eq. (14) has been verified through experimental measurements [50].

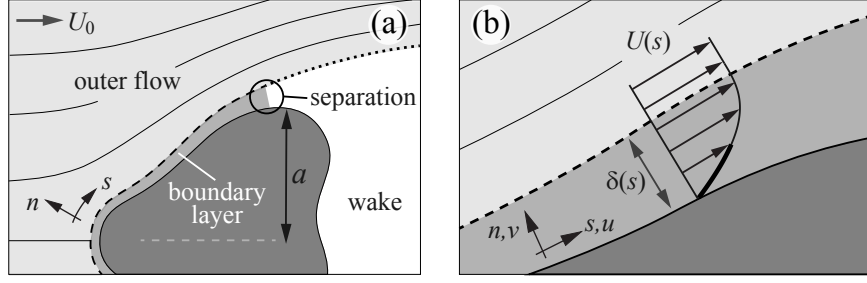


Figure 2: Prandtl decomposition of separated flow past a bluff body. (a) The flow can be decomposed into an outer component, a boundary-layer component, and a wake. The boundary layer is indicated by the dashed line and the free streamline by the dotted line. (b) The flow inside the boundary layer must transition from the outer value  $U(s)$  to the no-slip condition at the surface. Figure adapted from Moore et al. 2013 with permission [42].

### 3 The Prandtl flow model

We now introduce our model to describe the high-Reynolds-number, separated flow surrounding the body. Rather than attempt to resolve this flow directly through Eqs. (1)–(4), we make use of the so-called Prandtl decomposition. The idea is to partition the domain into an inner, outer, and wake region as illustrated in Fig. 2. In the outer region, the flow is assumed to be inviscid and irrotational, and can therefore be described by a velocity potential  $(u_o, v_o) = U_0 \nabla \phi$ , that satisfies

$$\nabla^2 \phi = 0, \quad (15)$$

$$\frac{\partial \phi}{\partial n} = 0 \quad \text{on } \partial B, \quad (16)$$

$$\nabla \phi \rightarrow (1, 0) \quad \text{as } |\mathbf{x}| \rightarrow \infty. \quad (17)$$

Equation (16) is the no-penetration condition on the body and Eq. (17) is the far-field condition. Since the outer flow is inviscid, a slip velocity  $U$  is permitted on the body surface,

$$U(s) = U_0 \left. \frac{\partial \phi}{\partial s} \right|_{\partial B}, \quad (18)$$

where  $s$  is arc length measured from the front stagnation point.

To account for the presence of the wake, we use a technique known as free-streamline theory (FST) [30, 3, 42]. This theory supposes that free streamlines emanate from the body to separate the outer region from the wake, as illustrated in Fig. 2(a). In FST, the outer flow and the paths  $\gamma$  of the free streamlines must be determined simultaneously. How the wake is modeled can vary, and, here, we take the simplest form in which the pressure is assumed to be constant inside the wake [42]. From this assumption, the steady Bernoulli equation implies that the velocity matches  $U_0$  on the free streamlines. In addition, the flow cannot penetrate the free streamlines, yielding the

two boundary conditions

$$\left. \frac{\partial \phi}{\partial n} \right|_{\gamma} = 0, \quad (19)$$

$$\left. \frac{\partial \phi}{\partial s} \right|_{\gamma} = 1. \quad (20)$$

Both of these conditions are required because  $\gamma$  is a free boundary (i.e. unknown a priori).

The inner region consists of a thin boundary layer surrounding the body, where the flow must transition to match the no-slip condition on the surface, as shown in Fig. 2(b). Due to the sharp transition, viscous effects cannot be ignored in this region. Scaling analysis of the Navier-Stokes equations produces the Prandtl boundary-layer equations [49, 53],

$$u \frac{\partial u}{\partial s} + v \frac{\partial u}{\partial n} - \nu \frac{\partial^2 u}{\partial n^2} = UU', \quad (21)$$

$$\frac{\partial u}{\partial s} + \frac{\partial v}{\partial n} = 0, \quad (22)$$

where  $(u, v)$  are the tangential and normal components of the *inner* flow. These equations hold within a boundary layer having characteristic thickness

$$\delta^* = \sqrt{\frac{\nu a}{U_0}}. \quad (23)$$

We note that the Eqs. (21)–(22) are nonlinear PDEs that depend on the outer flow  $U = U(s)$  and its derivative  $U' = dU/ds$ . These equations are supplemented by the boundary conditions

$$u(s, 0) = v(s, 0) = 0, \quad (24)$$

$$u(s, n) \rightarrow U(s) \quad \text{as } n/\delta^* \rightarrow \infty, \quad (25)$$

$$\frac{\partial^2 u}{\partial n^2}(s, 0) = -\frac{1}{\nu} U(s) U'(s). \quad (26)$$

The first is simply the boundary condition of vanishing velocity, and the second is a matching condition for the inner and outer flows. The third equation, a compatibility condition, results from evaluating Eq. (21) at  $n = 0$  and enforcing Eq. (24).

Similar scaling analysis can be applied to Eqs. (6)–(8) and Eqs. (10)–(12) for the concentration and temperature fields respectively [53]. For concentration, this gives

$$u \frac{\partial C}{\partial s} + v \frac{\partial C}{\partial n} = D \frac{\partial^2 C}{\partial n^2}, \quad (27)$$

$$C(s, 0) = 1, \quad (28)$$

$$C(s, n) \rightarrow 0 \quad \text{as } n/\delta^* \rightarrow \infty, \quad (29)$$

and for temperature,

$$u \frac{\partial T}{\partial s} + v \frac{\partial T}{\partial n} = \alpha \frac{\partial^2 T}{\partial n^2} + \frac{\nu}{c_p} \left( \frac{\partial u}{\partial n} \right)^2, \quad (30)$$

$$T(s, 0) = T_0, \quad (31)$$

$$T(s, n) \rightarrow T_0 + \Delta T \quad \text{as } n/\delta^* \rightarrow \infty. \quad (32)$$

These fields are confined to boundary layers,  $\delta_c$  and  $\delta_t$  respectively, which are typically smaller than  $\delta^*$ . The relative size of the boundary layers can be estimated by the Prandtl numbers [53],

$$\text{Pr}_c = \nu/D, \quad \text{Pr}_t = \nu/\alpha, \quad (33)$$

for concentration and temperature respectively. For solidified sugar dissolving in water, for example, the Prandtl number is  $\text{Pr}_c \sim 10^3$ , and the ratio of boundary layers can be estimated as  $\delta_c/\delta^* \sim \text{Pr}_c^{-1/3} \sim 0.1$ . Meanwhile, for ice melting in water,  $\text{Pr}_t \sim 10$ , giving a ratio of  $\delta_t/\delta^* \sim \text{Pr}_t^{-1/3} \sim 0.5$ .

We note that the last term in Eq. (30) represents heating from viscous dissipation, and its relative importance can be estimated by the Eckert number  $\text{Ec} = U_0^2/(c_p \Delta T)$  [53]. The specific heat of water is  $c_p = 4.2 \cdot 10^7$  erg/(g°C) (cgs units), and, consequently, Ec is very small in many laboratory experiments [25, 50, 42, 27]. We will therefore neglect dissipative heating in the following, although we point out that this effect may be important in some natural examples, such as meteors ablating in the atmosphere [21, 33].

## 4 Analysis within the boundary layer

In this section, we present some analysis of the boundary-layer equations, (21)–(26), that will eventually be used to find the bodies of self-similar dissolution, melting, and erosion. This analysis makes use of the Falkner-Skan similarity solutions of boundary-layer theory [49]. For the inner flow, we introduce a stream function  $\psi_i$  such that  $u = \partial_n \psi_i$  and  $v = -\partial_s \psi_i$ . In terms of  $\psi_i$ , the Prandtl equations (21)–(22) become

$$\frac{\partial \psi_i}{\partial n} \frac{\partial^2 \psi_i}{\partial n \partial s} - \frac{\partial \psi_i}{\partial s} \frac{\partial^2 \psi_i}{\partial n^2} - \nu \frac{\partial^3 \psi_i}{\partial n^3} = UU'. \quad (34)$$

Near the front stagnation point,  $s = 0$ , we suppose that the outer flow is prescribed by a power law  $U(s) \propto s^m$ . We introduce the similarity transform  $\psi_i = \sqrt{\nu s U} f(\eta)$ , where  $\eta = n/\sqrt{\nu s/U(s)}$ , which gives the ordinary differential equation (ODE) for  $f(\eta)$ ,

$$f''' + \frac{1}{2}(m+1)ff'' - mf'^2 + m = 0. \quad (35)$$

The solution of this ODE (subject to boundary conditions) completely determines the inner flow as long as  $U(s)$  follows a power law.

As discussed earlier, the concentration and temperature fields are typically confined to boundary layers even smaller than  $\delta^*$  (so long as  $\text{Pr}_c > 1$  and  $\text{Pr}_t > 1$ ). Therefore, to determine the evolution of these fields, only the *inner* flow is required in Eqs. (27)–(29) and (30)–(32). Supposing that the solute concentration can be represented by the same similarity variable, i.e.  $C(s, n) = \theta(\eta)$ , gives

$$\theta'' + \frac{1}{2}\text{Pr}_c(m+1)f\theta' = 0, \quad (36)$$

$$\theta(0) = 1, \quad \lim_{\eta \rightarrow \infty} \theta(\eta) = 0. \quad (37)$$

The temperature field is also governed by the above equations, except with  $\theta$  defined by  $T(s, n) = T_0 + \Delta T(1 - \theta(\eta))$ , and with  $\text{Pr}_t$  replacing  $\text{Pr}_c$ . From Eqs. (5) and (9), the interface velocities for

dissolution and melting are then given by

$$V_n^{(D)} = D \sqrt{\frac{U(s)}{\nu s}} \theta'(0), \quad (38)$$

$$V_n^{(M)} = \frac{\alpha c_p \Delta T}{L} \sqrt{\frac{U(s)}{\nu s}} \theta'(0). \quad (39)$$

Thus, as long as  $\text{Pr}_c > 1$  and  $\text{Pr}_t > 1$ , dissolution and melting are represented by the same set of equations, with the only difference being in the parameter values. Erosion, on the other hand, depends on the surface shear stress,  $\tau_s$ , defined in Eq. (13). Using the similarity solution for  $\psi_i$  gives

$$\tau_s(s) = \sqrt{\frac{\rho \mu U(s)^3}{s}} f''(0). \quad (40)$$

The interface velocity for erosion is then

$$V_n^{(E)} = -C_E \left| \sqrt{\frac{\rho \mu U(s)^3}{s}} f''(0) \right|. \quad (41)$$

where  $f''(0)$  can be found through numerical integration of Eq. (35) if desired.

As suggested previously [50, 42, 27], we propose that the morphologies formed during dissolution, melting, and erosion are those for which material removal is *uniform* along the surface, since such a shape would naturally maintain itself during the shrinking process. To find these shapes, we therefore require the interface velocities in Eqs. (38), (39), and (41) to be independent of  $s$ . In each case, this requirement simply reduces to a condition on the outer flow,

$$U(s) \propto s \quad \text{for uniform dissolution or melting}, \quad (42)$$

$$U(s) \propto s^{1/3} \quad \text{for uniform erosion}. \quad (43)$$

Thus, for uniform dissolution or melting, the outer flow must increase linearly with distance from the front stagnation point, and for uniform erosion it must increase with a  $1/3$  power law. These equations provide a tremendous simplification in seeking the equilibrium shapes of interest, since they neatly encapsulate the details of the boundary-layer flow through a condition on the *outer* flow alone.

Before attempting to impose Eqs. (42) and (43) generally, we note a few simple arrangements that satisfy them [49]. First, flow impinging orthogonally on an infinite, flat wall satisfies  $U(s) \propto s$ , and therefore this configuration would be maintained during dissolution or melting. Second, an infinite wedge with an opening angle of  $90^\circ$  pointing into the flow satisfies  $U(s) \propto s^{1/3}$ , and would thus erode uniformly. Despite being *infinite* bodies, these configurations provide useful shape information near a front stagnation point. In particular, they predict the front to remain locally flat during dissolution/melting, but to form a right angle during erosion. As seen in Fig. 1, both of these features are indeed observed in experiments [50, 42, 27]. The infinite configurations, however, do not predict how shape varies away from the stagnation point. An important insight is that, since our boundary-layer analysis only relies on knowing  $U(s)$  and not on shape directly, the conditions for self-similar shrinking (42)–(43) remain unchanged when considering bodies of *finite* extent.

## 5 Free-streamline theory giving rise to Riemann-Hilbert problems

We now introduce the FST method used to solve for the separated flow around a finite body [30, 3, 42]. We identify physical space with the complex plane  $z = x + iy$  and introduce the complex potential  $w(z) = \phi + i\psi$ . Here,  $\phi$  and  $\psi$  are the potential and stream function of the outer flow, where  $\phi$  must satisfy Eqs. (15)–(17) and (19)–(20). The outer velocity field,  $(u_o, v_o)$ , is given by

$$u_o - iv_o = U_0 \frac{dw}{dz}. \quad (44)$$

We introduce the log-hodograph variable  $F$ , defined as

$$F(z) = i \log \frac{dw}{dz}. \quad (45)$$

$F = \Phi + i\Psi$  is an analytic function, which relates to the velocity field through

$$u_o - iv_o = U_0 \exp(-iF) = U_0 \exp(\Psi) \exp(-i\Phi). \quad (46)$$

As seen in this equation,  $\Psi(x, y)$  determines the local speed of the outer flow and  $\Phi(x, y)$  its local direction. In particular, since the outer flow must be tangential to the surface, evaluating  $\Phi$  on the boundary encodes the shape of the body through its local tangent vector (illustrated in the left panel of Fig. 3). Our overall strategy is to use conditions (42)–(43) on flow speed,  $\Psi$ , to determine  $\Phi$  and thus uncover the equilibrium shapes of interest.

Conditions (42) and (43) can each be expressed as a power law

$$U(s) = U_0(s/s_0)^m, \quad (47)$$

where  $m = 1$  or  $1/3$ . Here,  $s_0$  is the point of flow separation and we have chosen the proportionality constants from Eqs. (42) and (43) to satisfy Eq. (20) at  $s_0$ . Using Eq. (46), we then obtain the boundary condition for  $\Psi$ ,

$$\Psi = m \log |s/s_0| \quad \text{on } \partial B, \quad (48)$$

where  $m = 1$  for uniform dissolution/melting and  $m = 1/3$  for uniform erosion. We are now considering  $s$  to be the *signed* distance from the front stagnation point, with  $s > 0$  corresponding to the upper portion of the body.

Following the FST method [42], we conformally map  $z$  in the physical domain to  $\zeta$  in the interior of the upper-half disk (UHD) via

$$\frac{dz}{d\zeta} = \frac{1}{2} c_0 \exp(iF) (\zeta - 1/\zeta^3), \quad (49)$$

where  $c_0$  is a constant to be determined later. This mapping is illustrated in Fig. 3. The surface of the body, parameterized by  $s$ , maps to the perimeter of the UHD,  $\zeta = \exp(i\theta)$ , via

$$\frac{ds}{d\theta} = c_0 \exp(-\Psi) |\sin 2\theta|. \quad (50)$$

In addition, we specify the following special values of the map

$$s = 0 \leftrightarrow \theta = \pi/2, \quad s = s_0 \leftrightarrow \theta = \pi, \quad s = -s_0 \leftrightarrow \theta = 0. \quad (51)$$

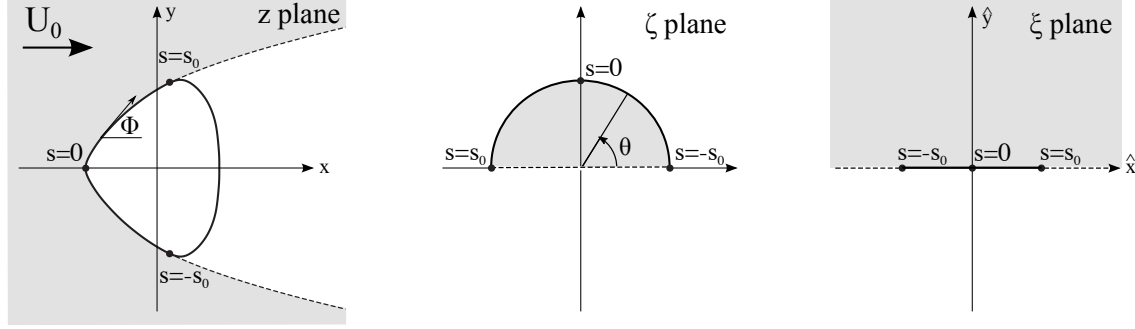


Figure 3: The conformal maps. A point  $z$  in the physical domain is first mapped to  $\zeta$  in the upper-half disk and then to  $\xi$  in the upper-half plane. In each domain, the bold and dashed lines indicate the mapped positions of the body surface and the free streamlines respectively;  $s = 0$  corresponds to the front stagnation point and  $s = \pm s_0$  to the separation points. In the physical domain (left), the value  $\Phi$  encodes the shape of the body through the local tangent angle.

The up-down symmetry in the physical domain implies that  $s(\theta)$  has odd symmetry about  $\theta = \pi/2$ . Using Eq. (48), and WLOG considering only the upper portion of the body gives

$$\frac{ds}{d\theta} = -c_0(s/s_0)^{-m} \sin 2\theta \quad \text{for } \theta \in (\pi/2, \pi), s \in (0, s_0). \quad (52)$$

This separable ODE has solution

$$(s/s_0)^{m+1} = \cos^2 \theta \quad \text{for } \theta \in (\pi/2, \pi), s \in (0, s_0). \quad (53)$$

Here, we have used the special values from Eq. (51) to determine  $c_0$  as well as a constant of integration. The remainder of the map, i.e.  $s(\theta)$  for  $\theta \in (0, \pi/2)$ , can be obtained by odd reflection. Inserting Eq. (53) into Eq. (48), gives boundary data for  $\Psi$  on the UHD perimeter,

$$\Psi = \frac{2m}{m+1} \log |\cos \theta| \quad \text{for } \zeta = e^{i\theta}, \theta \in [0, \pi], \quad (54)$$

which has a logarithmic singularity at  $\theta = \pi/2$ . Meanwhile, under transformation (49), the free streamlines,  $z \in \gamma$ , map to the segment  $\zeta \in (-1, 1)$ , and thus Eq. (20) yields the additional boundary condition

$$\Psi = 0 \quad \text{for } \zeta \in (-1, 1). \quad (55)$$

Given boundary conditions (54) and (55) on  $\Psi$ , we seek the boundary values of  $\Phi$ , which will produce the equilibrium shapes of interest. This task of determining  $\Phi$  from boundary data of its harmonic conjugate is known as a Riemann-Hilbert problem<sup>2</sup> [1, 43].

We remark that imposing conditions on the flow speed,  $\Psi$ , renders Eq. (50) *explicit*, which allowed us to obtain the boundary map  $s \leftrightarrow \theta$  given by Eq. (53). This is in contrast to the classical FST problem of determining the flow around a body of known shape. In that case, boundary data is prescribed on flow direction,  $\Phi$ , but not on flow speed,  $\Psi$ , and so the the mapping  $s \leftrightarrow \theta$  is an unknown that must be solved for. Thus, while the classical FST problem usually requires numerical

solution, we will show that the *inverse* problem - that of determining body shape from conditions placed on the flow - is amenable to exact solution through the RH framework.

## 6 Exact solutions to the Riemann-Hilbert problems

In this section, we construct a class of exact solutions to the RH problems given by Eqs. (54)–(55). We first conformally map  $\zeta$  in the UHD to  $\xi = \hat{x} + i\hat{y}$  in the upper-half plane (UHP) through

$$\xi = -\frac{1}{2}(\zeta + 1/\zeta). \quad (56)$$

As illustrated in Fig. 3, the perimeter of the UHD,  $\zeta = e^{i\theta}$ , maps to the real segment  $\hat{x} \in [-1, 1]$ , and the diameter of the UHD  $\zeta \in (-1, 1)$  maps to  $\hat{x} \in (-\infty, -1) \cup (1, \infty)$ . In the UHP, boundary conditions (54)–(55) become

$$\Psi(\hat{x}) = \frac{2m}{m+1} \log |\hat{x}| \quad \text{for } \hat{x} \in [-1, 1], \quad (57)$$

$$\Psi(\hat{x}) = 0 \quad \text{for } \hat{x} \in (-\infty, -1) \cup (1, \infty). \quad (58)$$

To solve the RH problem, we need to determine  $\Phi(\hat{x})$  on the real line.

We first make a few observations. Since  $\Phi$  corresponds to the local flow direction, the up-down symmetry in the physical domain implies that  $\Phi(\hat{x})$  has odd symmetry. Furthermore, the logarithmic singularity in Eq. (57) gives rise to a jump discontinuity in  $\Phi(\hat{x})$  across  $\hat{x} = 0$  (corresponding to the front stagnation point). This relationship is demonstrated in Figs. 4(a)–(b). The size of the jump is set by the strength of the singularity, giving

$$\Phi(0^+) - \Phi(0^-) = \frac{2\pi m}{m+1}. \quad (59)$$

This jump, since it corresponds to the change in flow direction across the stagnation point, determines the opening angle of the equilibrium body. We illustrate this idea in Figs. 4(c)–(d). The condition for uniform dissolution/melting is  $m = 1$ , for which Eq. (59) gives a jump of  $\pi$ . The flow, therefore, changes direction by  $180^\circ$  as it crosses the stagnation point, meaning the body has a flat front surface as shown in Fig. 4(c). Uniform erosion, on the other hand, requires  $m = 1/3$ , which gives a jump of  $\pi/2$  and thus corresponds to a right-angled nose as shown in Fig. 4(d). Equation (59) is therefore consistent with the infinite configurations discussed in §4 and provides an alternative derivation of those results.

To determine how shape varies away from the stagnation point, we now seek  $\Phi(\hat{x})$  on the remainder of the real line. Since  $\Phi$  and  $\Psi$  are harmonic conjugates, their boundary values are related by the real-line Hilbert transform [58, 43]

$$\Phi(\hat{x}) = \frac{1}{\pi} \int_{-\infty}^{\infty} \frac{\Psi(t)}{t - \hat{x}} dt, \quad (60)$$

---

<sup>2</sup>This is arguably the simplest formulation of a RH problem, in which data is prescribed on a boundary as opposed to a jump condition being prescribed across a boundary. Although the later has perhaps been more commonly associated with the RH name in recent years, the two formulations can be shown to be equivalent through a Schwarz reflection (see [43], Chap. 5).

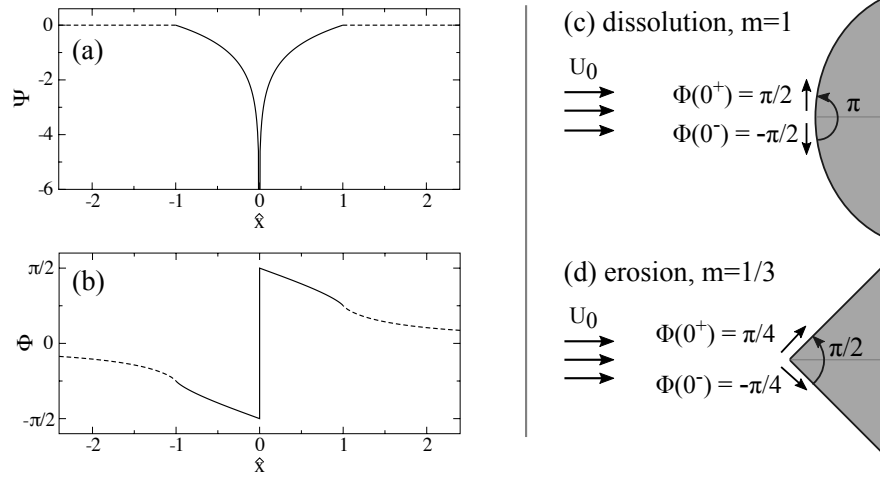


Figure 4: (a)–(b) The Hilbert transform maps boundary data of  $\Psi$  to that of  $\Phi$ , where the logarithmic singularity in  $\Psi$  gives rise to a jump discontinuity in  $\Phi$ . The solid and dashed lines correspond to the body surface and the free streamlines respectively. (c)–(d) The jump in  $\Phi$  dictates the opening angle of the equilibrium shape. (c) For dissolution/melting, the flow changes direction by  $\pi$  across the stagnation point, corresponding to a flat front surface. (d) For erosion, the direction change is  $\pi/2$ , corresponding to a right angle.

where  $\oint$  indicates a Cauchy principle value. Inserting boundary conditions (57)–(58) gives

$$\Phi(\hat{x}) = \frac{2m}{\pi(m+1)} \int_{-1}^1 \frac{\log|t|}{t - \hat{x}} dt, \quad (61)$$

where the integration domain has been truncated since  $\Psi(\hat{x})$  vanishes outside of the interval  $[-1, 1]$ . Integrating Eq. (61) by parts, differentiating under the integration sign, and then evaluating the result by partial fraction decomposition gives a closed-form expression for  $d\Phi/d\hat{x}$ ,

$$\frac{d\Phi}{d\hat{x}} = \frac{2m}{\pi(m+1)} \frac{1}{\hat{x}} \log \left| \frac{1-\hat{x}}{1+\hat{x}} \right|. \quad (62)$$

For the purpose of antiderentiating Eq. (62), we introduce the dilogarithm function [2, 61],

$$\text{Li}_2(z) = - \int_0^z \frac{\log(1-z')}{z'} dz' \quad \text{for } z \in \mathbb{C} \setminus [1, \infty). \quad (63)$$

We will use the odd part of this function<sup>3</sup>, denoted  $\tilde{\text{Li}}_2(\hat{x}) = (\text{Li}_2(\hat{x}) - \text{Li}_2(-\hat{x}))/2$ . The antiderivative of Eq. (62) can then be expressed as

$$\Phi(\hat{x}) = \frac{4m}{\pi(m+1)} \left( \frac{\pi^2}{4} \text{sgn}(\hat{x}) - \tilde{\text{Li}}_2(\hat{x}) \right) \quad \text{for } \hat{x} \in [-1, 1], \quad (64)$$

<sup>3</sup>This function has the power series representation  $\tilde{\text{Li}}_2(\hat{x}) = \sum_{k=0}^{\infty} \hat{x}^{2k+1}/(2k+1)^2$  for  $-1 \leq \hat{x} \leq 1$ , which is convenient for numerical evaluation.

where we have used the odd symmetry of  $\Phi(\hat{x})$  and the jump condition (59) to determine the integration constants on both sides of  $\hat{x} = 0$ . To evaluate  $\Phi(\hat{x})$  for  $|\hat{x}| > 1$ , we note that Eq. (62) possesses the following symmetry

$$\frac{d}{d\hat{x}}\Phi(1/\hat{x}) = -\frac{d}{d\hat{x}}\Phi(\hat{x}), \quad (65)$$

which, upon ensuring continuity across  $\hat{x} = 1$ , gives

$$\Phi(\hat{x}) = \frac{4m}{\pi(m+1)} \tilde{\text{Li}}_2(1/\hat{x}) \quad \text{for } \hat{x} \in (-\infty, -1) \cup (1, \infty). \quad (66)$$

Equations (64) and (66) complete the solution of the RH problem in the UHP.

To illustrate the basic behavior of these solutions, we show in Figs. 4(a)–(b) the boundary data,  $\Psi(\hat{x})$ , and the resulting solution,  $\Phi(\hat{x})$ , for the case  $m = 1$ . The figure demonstrates the relationship between the logarithmic singularity in  $\Psi$  and the jump discontinuity in  $\Phi$ . In the physical domain,  $\Phi$  corresponds to the local tangent direction, where the interval  $\hat{x} \in [-1, 1]$  corresponds to the body surface (solid line) and  $\hat{x} \in (-\infty, -1) \cup (1, \infty)$  to the free streamlines (dashed lines). To evaluate Eqs. (64) and (66) for any other value of  $m$ , it suffices to simply rescale the solutions shown in the figure.

## 7 The equilibrium shapes

We now use solutions (64) and (66) to obtain the geometries of self-similar dissolution, melting, and erosion. To begin, a smooth boundary in two dimensions can be parameterized by its arc length,  $(x(s), y(s))$ . In the physical domain,  $\Phi$  corresponds to the local direction of the outer flow, which, on the body surface, must align with the tangent vector  $(\partial_s x, \partial_s y)$ . Equation (46) then gives

$$\frac{\partial x}{\partial s} = \cos \Phi, \quad \frac{\partial y}{\partial s} = \sin \Phi. \quad (67)$$

Therefore,  $\Phi$  can be interpreted as the *angle* formed by the body's tangent vector with the horizontal (see the left panel of Fig. 3). To obtain the equilibrium geometries, we need only evaluate  $\Phi$  in the physical domain, i.e. the  $z$ -plane, and use the result to integrate Eq. (67).

Conformal maps (49) and (56) yield the following relations between the boundaries of the UHP and of the physical domain

$$\hat{x} = \text{sgn}(s) |s/s_0|^{\frac{m+1}{2}} \quad \text{for } |s| \leq s_0, \quad (68)$$

$$\hat{x} = \text{sgn}(s) \sqrt{(m+1)|s/s_0| - m} \quad \text{for } |s| > s_0. \quad (69)$$

Inserting these relations into Eqs. (64) and (66) gives  $\Phi$  in the physical domain

$$\Phi = \frac{4m \text{sgn}(s)}{\pi(m+1)} \left( \frac{\pi^2}{4} - \tilde{\text{Li}}_2 \left( |s/s_0|^{\frac{m+1}{2}} \right) \right) \quad \text{for } s \in [-s_0, s_0], \quad (70)$$

$$\Phi = \frac{4m \text{sgn}(s)}{\pi(m+1)} \tilde{\text{Li}}_2 \left( 1/\sqrt{(m+1)|s/s_0| - m} \right) \quad \text{for } s \in (-\infty, -s_0) \cup (s_0, \infty). \quad (71)$$

Equations (70) and (71) thus provide the *local tangent angle as a function of arc length* on the surface of the body and on the free streamlines respectively. In particular, setting  $m = 1$  in Eq. (70) produces the shape of self-similar dissolution/melting,

$$\Phi = \frac{\pi}{2} \operatorname{sgn}(s) - \frac{2}{\pi} \tilde{\text{Li}}_2(s/s_0) \quad \text{for } s \in [-s_0, s_0], \quad (72)$$

and  $m = 1/3$  the shape of self-similar erosion,

$$\Phi = \frac{1}{\pi} \operatorname{sgn}(s) \left( \frac{\pi^2}{4} - \tilde{\text{Li}}_2 \left( |s/s_0|^{\frac{2}{3}} \right) \right) \quad \text{for } s \in [-s_0, s_0]. \quad (73)$$

In Figs. 5(a)–(b), we show these two equilibrium shapes, obtained by inserting  $\Phi$  into Eq. (67) and integrating numerically. To visualize the surrounding flow, we also show the streamlines as computed by a legacy FST code [42].

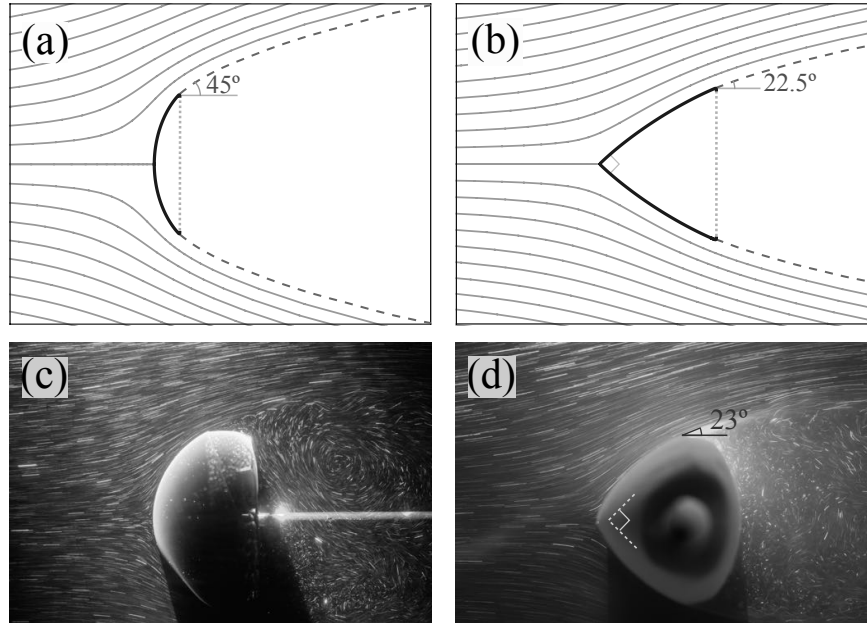


Figure 5: The equilibrium morphologies. (a)–(b) The shapes predicted by the RH solutions for (a) dissolution/melting and (b) erosion, along with surrounding streamlines as computed by FST. The dashed lines indicate the *free streamlines*. The flow separates at an angle of  $45^\circ$  in the case of dissolution/melting and  $22.5^\circ$  in the case of erosion. (c)–(d) Morphologies seen to develop experimentally during flow-driven (c) dissolution and (d) erosion. (d) The nose of the eroding body can be compared to a right angle (dashed white) and the measured flow-separation angle is  $23^\circ$ .

As seen in Fig. 5(a), the body of self-similar dissolution/melting has a locally flat front, in agreement with the infinite-extent configurations of §4 and with the jump condition (59). However, Eq. (72) provides additional information on how the surface curves away from the front stagnation point. Looking back at Fig. 4(b), we see that  $\Phi$  decreases nearly linearly for  $\hat{x} \in (0, 1)$ , and, in addition, the boundary map (68) is linear for  $m = 1$ . Together, these observations indicate a surface

of roughly constant curvature, and, indeed, the front of the body shown in Fig. 5(a) resembles a circular arc. Meanwhile, the body of self-similar erosion in Fig. 5(b) is distinguished by a right angle at its nose. This angle is consistent with §4, but, here too, the surface curves away from the stagnation point as cannot be predicted by the infinite-extent configurations. In both cases, we can determine the angle at which the flow separates by evaluating  $\Phi$  at  $s_0$  in Eqs. (72) and (73). Using the special value  $\tilde{L}i_2(1) = \pi^2/8$ , we get a separation angle of  $45^\circ$  in the case of dissolution/melting and  $22.5^\circ$  in the case of erosion, as shown in Figs. 5(a)–(b). Solutions (72) and (73) do not apply past flow separation, and in the figure we simply complete the bodies with a flat backside (faint dotted lines).

For comparison, we show in Figs. 5(c) and (d) experimental images of the shapes that develop during flow-driven dissolution and erosion, with the surrounding flows visualized by streakline photography. The images show that, indeed, dissolution creates a rounded front surface and erosion forms an approximate right-angled nose. The RH solutions not only capture these shapes, but also appear to describe the surrounding flow structures remarkably well. In particular, the angle of flow separation offers a precise prediction that can be compared with the experiments. We note that the dissolving body shown in Fig. 5(c) is axisymmetric and so only qualitative comparison with our 2D theory would be expected<sup>4</sup>. However, the eroding body shown in Fig. 5(d) is a cylindrical one, allowing for direct comparison. From the image, we measure the separation angle to be  $23^\circ \pm 3^\circ$ , which agrees closely with the predicted value of  $22.5^\circ$ . While both bodies also show some interesting features beyond flow separation, such features cannot be predicted by FST and would require direct numerical simulation to resolve the complex flow in the wake.

We briefly discuss how our dissolution/melting solution compares to the classical Ivantsov solution for a melting/solidifying front protruding into a liquid [32]. In that setting, the Ivantsov solution predicts a parabolic front to grow or recede self-similarly. This analysis has been extended to account for a background flow, in the case of porous-media flow (i.e. potential flow) [9, 15] and viscous Oseen flow (valid for small Reynolds numbers) [4]. At first glance, our analysis appears most closely related to the porous-media case, since both involve potential flows. However, porous-media flow is *unseparated* potential flow with *no viscous boundary layer*. It therefore permits a tangential velocity on the solid interface, whereas our viscous boundary layer prohibits this. The two flows, therefore, are not similar, even in the vicinity of a stagnation point. Our situation is actually more comparable to viscous Oseen flow [4]. In a small region near the front stagnation point, the high-speed flow considered here is well approximated by Stokes or Oseen flow [49]. Indeed, our interface solution, Eq. (72), can be approximated by a parabola there and, in this sense, is locally consistent with the Ivantsov solution. Further back on the body, the two solutions differ as the curvature of the Ivantsov solution decreases with distance while our solution maintains nearly constant curvature until flow separation. These morphological differences arise from the differences in the surrounding flows. Our solution applies to high-Reynolds-number flows where inertia dominates, while the Ivantsov solution applies to Oseen flows where inertia is relatively small [4].

## 8 Discussion

In this paper, we have developed a theoretical framework that links the processes of flow-driven dissolution, melting, and erosion. In each case, the development of morphology depends intimately

---

<sup>4</sup>Efforts to visualize the dissolution of cylindrical bodies experimentally proved difficult due to buoyancy and optical effects introduced by dissolving sugar.

on the physics within the boundary layer, but, importantly, the condition for *self-similar* evolution reduces to a requirement on the *outer* flow alone. This simplification leads to a class of Riemann-Hilbert problems whose exact solutions provide the equilibrium geometries of interest. Remarkably, the solutions capture the very different morphologies formed by dissolution/melting and erosion that have been observed in laboratory experiments.

Throughout the analysis, we have appealed to the idea that, in long time, a body should converge to the shape for which material removal is *uniform* along its surface. The agreement with experiments provides empirically support for this idea, but there are exceptions to the rule. In a recent study of erosion in *Stokes* flow, numerical simulations showed that, although there exists a shape of uniform shear stress, an eroding body does *not* converge to that shape [41]. In fact, the body does not converge to any limiting form and only becomes more and more slender as it vanishes. This example illustrates that uniform material removal is only an approximate condition for self-similarity. The exact condition requires the removal rate to balance surface curvature, as expressed in Eq. (A32) of Moore et al. 2013 [42]. As demonstrated by Mitchell & Spagnolie 2016, it is not always the case that such a morphology exists [41].

To enforce the exact self-similarity condition, it might be possible to derive an evolution equation for the conformal map between physical space (the  $z$ -plane) and the UHP (the  $\xi$ -plane), analogous to the Polubarnova-Galin equation for pure potential flow (i.e. unseparated flow with no viscous boundary layer) [26, 15, 14]. For the case of a protrusion melting or solidifying in a porous medium, this formulation was used to obtain a class of explicit solutions, rich enough to capture the behaviors of fingering, tip-splitting, and cusp formation [15]. Applying similar ideas to the present case of high-speed, *separated* flows with *viscous boundary layers* is an area for future research.

In the case of melting, we have neglected the effects of thermal expansion and of surface tension, since both are relatively small in typical macro-scale laboratory experiments [25]. These effects can, however, arise in other applications. Thermal expansion becomes significant at near-sonic or supersonic flow speeds - for example the air flows encountered by meteors ablating in the atmosphere [21, 33]. Meanwhile, the contribution of surface tension to the free energy plays a role in nucleation and dendrite formation [22, 47], where it has a stabilizing influence. In such instances, surface tension effects are modeled by the Gibbs-Thomson correction [22, 39, 47, 29], which modifies Eq. (11) to include a curvature term in the equilibrium melting temperature. If applied to the present analysis, such a term would smooth the equilibrium morphology shown in Fig. 5(a). In particular, it would round the sharp corners that exist at flow separation. It is not clear, however, if exact solutions could still be obtained were the Gibbs-Thomson term included.

Finally, we point out that the canonical problem considered here - that of a body undergoing material loss in a high-speed, unidirectional flow - incorporates many of the complexities found in natural settings, such as boundary layers, flow separation, and, crucially, the coupling of morphology and flow. As such, the results could be used to test, and perhaps even design, numerical methods for simulating flow-driven boundary motion in nature. Examples might include the evolution of coastal morphology or polar ice shelves. These examples involve more complex background flows, exhibiting both temporal and spatial variation across many scales. Despite these complexities, it may be possible to understand the emergence of morphology through similar principles, and this is a promising direction for future research.

## Acknowledgement

I would like to thank Stephen Childress, Jinzi Mac Huang, Kenneth McLaughlin, Ziad Musslimani, Leif Ristroph, Michael Shelley, Saverio Spagnolie, Esteban Tabak, and Jun Zhang for helpful discussions. This work was supported by the FSU First-Year Assistant Professor (FYAP) award: Project ID 036209, Fund Code 551.

## References

- [1] M.J. Ablowitz and A.S. Fokas. *Complex Variables: Introduction and Applications*. Cambridge University Press, 2003.
- [2] M. Abramowitz, I.A. Stegun, et al. Handbook of mathematical functions. *Applied Mathematics Series*, 55:62, 1966.
- [3] S. Alben, M. Shelley, and J. Zhang. How flexibility induces streamlining in a two-dimensional flow. *Phys. Fluids*, 16:1694–1713, 2004.
- [4] R. Ananth and W.N. Gill. Dendritic growth of an elliptical paraboloid with forced convection in the melt. *J. Fluid Mech.*, 208:575–593, 1989.
- [5] D.M. Anderson and M.G. Worster. Weakly nonlinear analysis of convection in mushy layers during the solidification of binary alloys. *J. Fluid Mech.*, 302:307–331, 1995.
- [6] Y.A. Antipov and V.V. Silvestrov. Method of Riemann surfaces in the study of supercavitating flow around two hydrofoils in a channel. *Physica D*, 235(1):72–81, 2007.
- [7] Y.A. Antipov and V.V. Silvestrov. Double cavity flow past a wedge. In *Proc. R. Soc. A*, volume 464, pages 3021–3038. The Royal Society, 2008.
- [8] Y.A. Antipov and A.Y. Zemlyanova. Motion of a yawed supercavitating wedge beneath a free surface. *SIAM J. Appl. Math.*, 70(3):923–948, 2009.
- [9] M. Benamar, P.H. Bouissou, and P. Pelce. An exact solution for the shape of a crystal growing in a forced flow. *J. Cryst. Growth*, 92(1):97–100, 1988.
- [10] C. Camporeale. Hydrodynamically locked morphogenesis in karst and ice flutings. *J. Fluid Mech.*, 778:89–119, 2015.
- [11] J. Crank. Free and moving boundary problems. *AMC*, 10:12, 1984.
- [12] D. Crowdy. Explicit solution of a class of Riemann–Hilbert problems. *Annales Universitatis Paedagogicae Cracoviensis Studia Mathematica*, 8(1):5–18, 2009.
- [13] D.G. Crowdy. Surfactant-induced stagnant zones in the Jeong–Moffatt free surface Stokes flow problem. *Phys. Fluids*, 25(9):092104, 2013.
- [14] L.J. Cummings, S.D. Howison, and J.R. King. Two-dimensional Stokes and Hele–Shaw flows with free surfaces. *Eur. J. Appl. Math.*, 10(06):635–680, 1999.

- [15] L.M. Cummings, Y.E. Hohlov, S.D. Howison, and K. Kornev. Two-dimensional solidification and melting in potential flows. *J. Fluid Mech.*, 378:1–18, 1999.
- [16] P. Deift. *Orthogonal Polynomials and Random Matrices: a Riemann-Hilbert approach*, volume 3. American Mathematical Soc., 2000.
- [17] P. Deift and X. Zhou. A steepest descent method for oscillatory Riemann–Hilbert problems. asymptotics for the MKdV equation. *Ann. Math.*, pages 295–368, 1993.
- [18] P.A. Deift, A.R. Its, and X. Zhou. A Riemann-Hilbert approach to asymptotic problems arising in the theory of random matrix models, and also in the theory of integrable statistical mechanics. *Ann. Math.*, pages 149–235, 1997.
- [19] A. Dokoumetzidis and P. Macheras. A century of dissolution research: from Noyes and Whitney to the biopharmaceutics classification system. *Int. J. Pharm.*, 321(1):1–11, 2006.
- [20] J. Escher, J. Prüss, and G. Simonett. Analytic solutions for a Stefan problem with Gibbs-Thomson correction. In *J. Reine Angew. Math.* Citeseer, 2003.
- [21] S. Feldman. On the instability theory of the melted surface of an ablating body when entering the atmosphere. *J. Fluid Mech.*, 6(01):131–155, 1959.
- [22] F. Gibou, R. Fedkiw, R. Caflisch, and S. Osher. A level set approach for the numerical simulation of dendritic growth. *J. Sci. Comp.*, 19(1-3):183–199, 2003.
- [23] R.C. Grabowski, I.G. Droppo, and G. Wharton. Erodibility of cohesive sediment: the importance of sediment properties. *Earth-Sci. Rev.*, 105(3):101–120, 2011.
- [24] M. Hadžić and S. Shkoller. Global stability and decay for the classical Stefan problem. *Comm. Pure and Appl. Math.*, 68(5):689–757, 2015.
- [25] Y.L. Hao and Y.X. Tao. Heat transfer characteristics of melting ice spheres under forced and mixed convection. *J. Heat Transf.*, 124(5):891–903, 2002.
- [26] S.D. Howison. Complex variable methods in Hele–Shaw moving boundary problems. *Eur. J. Appl. Math.*, 3(03):209–224, 1992.
- [27] J.M. Huang, M.N.J. Moore, and L. Ristroph. Shape dynamics and scaling laws for a body dissolving in fluid flow. *J. Fluid Mech.*, 765:R3, 2015.
- [28] H.E. Huppert. The fluid mechanics of solidification. *J. Fluid Mech.*, 212:209–240, 1990.
- [29] H.E. Huppert and M.G. Worster. Flows involving phase change. *Handbook of Environmental Fluid Dynamics*, edited by HJ Fernando, CRC Press, Boca Raton, 2012.
- [30] J. Hureau, E. Brunon, and P. Legallais. Ideal free streamline flow over a curved obstacle. *J. Comput. Appl. Math.*, 72(1):193–214, 1996.
- [31] A. Its. The Riemann–Hilbert problem and integrable systems. *Notices of the AMS*, 50(11):1389–1400, 2003.

- [32] G.P. Ivantsov. Temperature around a spheroidal, cylindrical and acicular crystal growing in a supercooled melt. In *Dokl. Akad. Nauk*, volume 58, pages 567–569, 1947.
- [33] V.N. Kalashnik, B.E. Killikh, G.I. Petrov, Y.V. Polezhaev, A.N. Smirnov, and Y.V. Chudetskii. On the shape of bodies ablating in a supersonic gas stream. *Fluid Dyn.*, 16(1):11–14, 1981.
- [34] S. Kamvissis, K.T.R. McLaughlin, and P.D. Miller. *Semiclassical Soliton Ensembles for the Focusing Nonlinear Schrödinger Equation (AM-154)*, volume 68. Princeton University Press, 2003.
- [35] R.F. Katz and M.G. Worster. Stability of ice-sheet grounding lines. In *Proc. R. Soc. A*, page rspa20090434. The Royal Society, 2010.
- [36] P. Kondratiuk and P. Szymczak. Steadily translating parabolic dissolution fingers. *SIAM J. Appl. Math.*, 75(5):2193–2213, 2015.
- [37] K.T.R. McLaughlin and X. Zhou. *Recent Developments in Integrable Systems and Riemann–Hilbert Problems: AMS Special Session, Integrable Systems and Riemann–Hilbert Problems, November 10–12, 2000, University of Alabama, Birmingham, Alabama*, volume 326. American Mathematical Soc., 2003.
- [38] P. Meakin and B. Jamtveit. Geological pattern formation by growth and dissolution in aqueous systems. In *Proc. R. Soc. A*, volume 466, pages 659–694. The Royal Society, 2010.
- [39] K. Mikula and D. Sevcovic. A direct method for solving an anisotropic mean curvature flow of plane curves with an external force. *Math. Method. Appl. Sci.*, 27(13):1545–1565, 2004.
- [40] P.J. Missel, L.E. Stevens, and J.W. Mauger. Reexamination of convective diffusion/drug dissolution in a laminar flow channel: accurate prediction of dissolution rate. *Pharm. Res.*, 21(12):2300–2306, 2004.
- [41] W.H. Mitchell and S.E. Spagnolie. Viscous erosion with a generalized traction integral equation. *arXiv preprint arXiv:1604.04560*, 2016.
- [42] M.N.J. Moore, L. Ristroph, S. Childress, J. Zhang, and M.J. Shelley. Self-similar evolution of a body eroding in a fluid flow. *Phys. Fluids*, 25(11):116602, 2013.
- [43] N.I. Muskhelishvili and J.R.M. Radok. *Singular Integral Equations: Boundary Problems of Function Theory and their Application to Mathematical Physics*. Courier Corporation, 2008.
- [44] S. Olver. A general framework for solving Riemann–Hilbert problems numerically. *Numer. Math.*, 122(2):305–340, 2012.
- [45] S. Olver and T. Trogdon. Nonlinear steepest descent and numerical solution of Riemann–Hilbert problems. *Comm. Pure Appl. Math.*, 67(8):1353–1389, 2014.
- [46] G. Parker and N. Izumi. Purely erosional cyclic and solitary steps created by flow over a cohesive bed. *J. Fluid Mech.*, 419:203–238, 2000.
- [47] M. Perez. Gibbs–Thomson effects in phase transformations. *Scripta Mater.*, 52(8):709–712, 2005.

- [48] J.P. Perkins, N.J. Finnegan, and S.L. de Silva. Amplification of bedrock canyon incision by wind. *Nat. Geosci.*, 8(4):305–310, 2015.
- [49] C. Pozrikidis. *Introduction to Theoretical and Computational Fluid Dynamics*. Oxford University Press, New York, 1997.
- [50] L. Ristroph, M.N.J. Moore, S. Childress, M.J. Shelley, and J. Zhang. Sculpting of an erodible body by flowing water. *P. Natl. Acad. Sci. USA*, 109(48):19606–19609, 2012.
- [51] L.I. Rubinshtein. *The Stefan problem*, volume 27. American Mathematical Soc., 1971.
- [52] C.H. Rycroft and M.Z. Bazant. Asymmetric collapse by dissolution or melting in a uniform flow. In *Proc. R. Soc. A*, volume 472, page 20150531. The Royal Society, 2016.
- [53] H. Schlichting. *Boundary Layer Theory*. McGraw-Hill (New York), 1960.
- [54] M.B. Short, J.C. Baygents, J.W. Beck, D.A. Stone, R.S. Toomey III, and R.E. Goldstein. Stalactite growth as a free-boundary problem: A geometric law and its platonic ideal. *Phys. Rev. Lett.*, 94(1):018501, 2005.
- [55] M.B. Short, J.C. Baygents, and R.E. Goldstein. A free-boundary theory for the shape of the ideal dripping icicle. *Phys. Fluids*, 18(8):083101, 2006.
- [56] M. Siegel. Influence of surfactant on rounded and pointed bubbles in two-dimensional Stokes flow. *SIAM J. Appl. Math.*, 59(6):1998–2027, 1999.
- [57] Johan Stefan. Über die theorie der eisbildung, insbesondere über die eisbildung im polarmeere. *Annalen der Physik*, 278(2):269–286, 1891.
- [58] F.G. Tricomi. *Integral Equations*, volume 5. Courier Corporation, 1957.
- [59] C.R. Vanier and C. Tien. Free convection melting of ice spheres. *AICHE Journal*, 16(1):76–82, 1970.
- [60] T.Y. Wu. Fish swimming and bird/insect flight. *Ann. Rev. Fluid Mech.*, 43:25–58, 2011.
- [61] D. Zagier. The dilogarithm function. In *Frontiers in number theory, physics, and geometry II*, pages 3–65. Springer, 2007.
- [62] A.Y. Zemlyanova and Y.A. Antipov. Single-spiral-vortex model for a cavitating elastic curvilinear foil. *SIAM J. Appl. Math.*, 72(1):280–298, 2012.